Check for updates

Advanced Materials

ADVANCED MATERIALS
www.advmat.de

RESEARCH ARTICLE

Membrane-Confined Proton Management Orchestrates Proton-Electron Transfer for Efficient Photocatalytic Hydrogen Peroxide Synthesis

Zhiwei Xing[1] | Chi Qiao[2] | Kunkun Ren[1] | Haitao Su[1,3] | Sai Wang[4] | Zhifeng Dai[2] | Yubin Xiong[2] | Xiangju Meng[1,3] | Shengqian Ma[5] | Qi Sun[1]

[1]Key Laboratory of Biomass Chemical Engineering of Ministry of Education, Zhejiang University, Hangzhou, China | [2]Key Laboratory of Surface & Interface Science of Polymer Materials of Zhejiang Province, School of Chemistry and Chemical Engineering, Zhejiang Sci-Tech University, Hangzhou, China | [3]State Key Laboratory of Soil Pollution Control and Safety, Department of Chemistry, Zhejiang University, Hangzhou, China | [4]Hangzhou Institute of Advanced Studies, Zhejiang Normal University, Hangzhou, China | [5]Department of Chemistry, University of North Texas, Denton, Texas, USA

Correspondence: Zhifeng Dai (Daizhif@zstu.edu.cn) | Xiangju Meng (mengxj@zju.edu.cn) | Qi Sun (sunqichs@zju.edu.cn)

Received: 9 January 2026 | **Revised:** 14 June 2026 | **Accepted:** 24 June 2026

Keywords: covalent-organic-framework membrane | hydrogen peroxide synthesis | membrane catalysis | photocatalysis | proton-coupled electron transfer

ABSTRACT

Coordinating proton and electron transport remains a central challenge in photocatalysis, particularly for H_2O_2 synthesis, where two-electron oxygen reduction requires synchronized proton delivery and charge transfer. Here, we report hydroxyl-functionalized three-dimensional covalent organic framework (COF) membranes that regulate proton-coupled electron transfer within ordered nanochannels. Phenolic hydroxyl groups are precisely embedded in the membrane pores as internal proton reservoirs, while the continuous COF framework provides pathways for photogenerated electron transport. By tuning hydroxyl density, the dihydroxylated COF-2OH membrane establishes an optimal proton-management microenvironment, promoting O_2 adsorption, charge separation, superoxide/*OOH intermediate formation, and dynamic proton recycling. Under one-sun irradiation in pure water and ambient air, COF-2OH achieves an H_2O_2 production rate of 21.79 mmol g^{-1} h^{-1} without sacrificial agents or cocatalysts, greatly outperforming the corresponding powder catalyst. Mechanistic experiments and simulations reveal that membrane confinement and hydroxyl-mediated proton buffering jointly synchronize proton and electron fluxes during continuous photocatalysis. The free-standing membrane can also be integrated into a tubular Al_2O_3-supported reactor for in situ H_2O_2-driven photo-Fenton degradation of organic pollutants. This work establishes proton-managing COF membranes as programmable reaction interfaces for efficient solar H_2O_2 production and integrated water treatment.

1 | Introduction

Proton-coupled electron transfer (PCET) is a central elementary process in natural photosynthesis, electrocatalysis and artificial photocatalysis, where chemical conversion is governed not only by the availability of protons and electrons but also by their spatial and temporal coordination [1–6]. At isolated molecular or catalytic sites, PCET can occur through local proton and electron transfer events. In heterogeneous photocatalysis, however, efficient operation under steady-state irradiation requires these local events to be sustained as continuous proton and electron fluxes across structurally complex interfaces. This requirement

Zhiwei Xing and Chi Qiao contributed equally to this work.

© 2026 Wiley-VCH GmbH

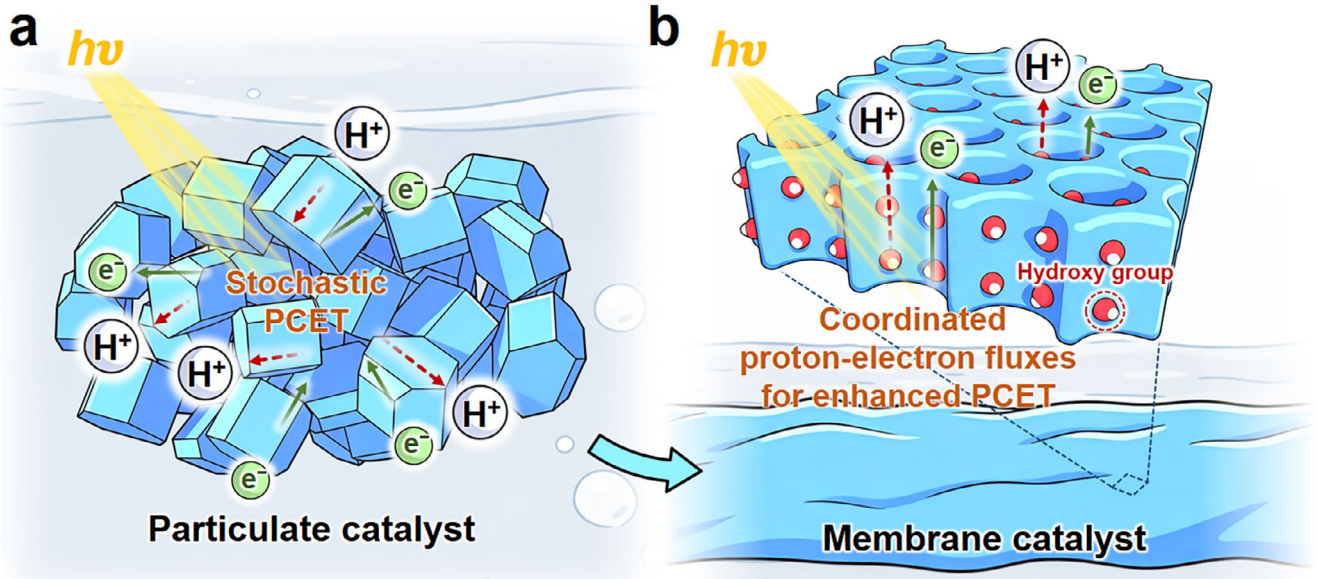


FIGURE 1 | Conceptual illustration of membrane-enabled coordination of PCET for efficient photocatalytic H_2O_2 synthesis. Schematic comparison showing the evolution of PCET from a stochastic, site-specific process in (a) particulate COF photocatalysts to a structure-defined and flux-coordinated process in (b) proton-managing COF membranes, where membrane confinement enables synchronized proton and electron transport.

is difficult to satisfy in conventional particulate photocatalysts, where proton transport, electron migration, and reactant activation usually occur through spatially disordered and weakly coupled pathways (Figure 1a). As a result, proton and electron delivery are often kinetically mismatched, leading to inefficient charge utilization, uncontrolled intermediate formation, and limited system-level regulation of PCET despite short local diffusion distances [7, 8].

Photocatalytic hydrogen peroxide (H_2O_2) synthesis provides a representative reaction in which these limitations become particularly evident [9–11]. H_2O_2 is an important green oxidant for chemical manufacturing, environmental remediation, and energy-related technologies, and its direct production from water and oxygen offers a sustainable alternative to the energy-intensive anthraquinone process [12–16]. The desired two-electron oxygen reduction pathway requires the concerted supply of electrons and protons to oxygen-derived intermediates, making H_2O_2 photosynthesis a typical PCET-governed reaction. In particulate photocatalysts, however, proton availability is generally dictated by random water dissociation, bulk solution composition or poorly defined surface groups, whereas photogenerated electrons migrate through locally heterogeneous domains. This uncoordinated proton/electron delivery not only suppresses the formation and stabilization of key *OOH or superoxide intermediates but also promotes charge recombination and competing oxygen-reduction pathways, thereby limiting both H_2O_2 productivity and selectivity [17–20].

Reorganizing photocatalysts into membrane architectures offers an opportunity to address this flux-coordination problem. Compared with particulate ensembles, membranes can provide continuous charge-transport pathways, spatially confined reaction environments, and stable gas-liquid-solid interfaces [21, 22]. In such systems, photogenerated electrons can be transported through an extended framework, while proton transfer can be confined and regulated within ordered nanochannels. This architectural feature creates the possibility of converting PCET from a locally stochastic process into a structure-guided and flux-coordinated process. Nevertheless, membrane confinement alone is insufficient to guarantee efficient PCET. Sustained photocatalysis requires internal proton-management elements that can buffer local proton concentration, release protons on demand and replenish proton reservoirs during continuous operation, thereby matching proton supply with photogenerated electron flux.

Covalent organic frameworks (COFs) are well suited for constructing such proton-managing membranes. Their crystalline frameworks, tunable pore chemistry, and extended π-conjugation allow functional groups to be positioned with molecular-level precision inside ordered channels [23–35]. When fabricated as free-standing membranes, COFs further combine defined nanochannels with continuous framework connectivity, enhanced light harvesting, and interfacial accessibility for gas and liquid reactants [22, 36–41]. Despite these advantages, microenvironment engineering in crystalline framework photocatalysts has so far been developed mainly in powder-based systems, where performance improvements are typically achieved through active-site modification, band-structure tuning or the use of external additives [42–44]. The rational use of intrinsic proton reservoirs embedded within continuous COF membrane channels to regulate PCET remains largely unexplored. This gap is reflected in the performance of many reported photocatalytic H_2O_2 systems, which commonly deliver production rates below approximately 1–10 mmol g^{-1} h^{-1} under simulated sunlight and often require sacrificial agents or cocatalysts (Table S1) [45–55].

Here, we report a series of hydroxyl-functionalized three-dimensional COF membranes as a platform for membrane-confined PCET regulation. Phenolic hydroxyl groups are systematically incorporated into ordered COF nanochannels to serve as internal proton reservoirs, while the continuous COF

15214095, 2026, 46, Downloaded from https://advanced.onlinelibrary.wiley.com/doi/10.1002/adma.73980 by Shengqian Ma - University Of North Texas Willis Library , Wiley Online Library on [21/10/2026]. See the Terms and Conditions (https://onlinelibrary.wiley.com/terms-and-conditions) on Wiley Online Library for rules of use; OA articles are governed by the applicable Creative Commons License

framework provides pathways for photogenerated electron transport (Figure 1b). By tuning the hydroxyl density, local proton availability can be matched with electron flux during photocatalytic H_2O_2 synthesis. The optimally dihydroxylated COF membrane promotes O_2 adsorption, facilitates charge separation, stabilizes oxygen-reduction intermediates and establishes a dynamic proton-recycling environment within confined nanochannels. As a result, the COF-2OH membrane achieves an H_2O_2 production rate of 21.79 mmol g^{-1} h^{-1} under one-sun irradiation in pure water, without sacrificial agents or cocatalysts, exceeding the corresponding COF powder catalyst by more than 60-fold. These results establish proton-managing COF membranes as a general strategy for coordinating proton and electron fluxes in photocatalysis and provide a membrane-based design principle for efficient solar-to-chemical conversion.

2 | Results and Discussion

2.1 | Membrane Synthesis and Characterizations

To enable controllable and coordinated PCET while minimizing extraneous structural variables, a series of free-standing COF membranes were rationally designed and synthesized via a reticular chemistry approach. The membrane architecture was deliberately adopted to impose spatially confined yet continuous transport pathways, providing a well-defined platform for flux-controlled PCET regulation. The COF membranes were prepared through acid-catalyzed Schiff-base condensation at a liquid-liquid interface between 4,4′,4″,4‴-(methanetetrayl)tetraaniline (TAM) and a series of aldehyde monomers bearing systematically varied hydroxyl substituents: 1,3,5-benzenetricarboxaldehyde, 2-hydroxy-1,3,5-benzenetricarboxaldehyde, 2,4-dihydroxy-1,3,5-benzenetricarboxaldehyde, and triformylphloroglucinol. The reactions were conducted at 35°C, with the aldehyde monomers dissolved in a mixed organic phase (ethyl acetate and mesitylene) and TAM dispersed in an acidic aqueous phase. The resulting membranes are denoted COF-0OH, COF-1OH, COF-2OH, and COF-3CO (Figure 2a). All COF membranes are free-standing, optically uniform, and mechanically robust.

Systematic variation in hydroxyl content induces distinct color changes, from white (COF-0OH) to orange (COF-1OH), dark yellow (COF-2OH), and light yellow (COF-3CO), reflecting deliberate modulation of the electronic structure via hydroxyl functionalization (Figure 2b, inset). Scanning electron microscopy (SEM) reveals smooth, continuous, and defect-free surfaces, while atomic force microscopy (AFM) confirms homogeneous thicknesses of 205 ± 5 nm across all samples (Figure 2b,c), thereby enabling a direct and unbiased comparison of their PCET behaviors. Successful COF formation was verified by Fourier-transform infrared (FT-IR) and solid-state ^{13}C nuclear magnetic resonance (^{13}C NMR) spectroscopy. For COF-0OH, COF-1OH, and COF-2OH, the emergence of a characteristic imine (C═N) stretching vibration at ~1620 cm^{-1} confirms imine-linked networks. Weak residual carbonyl signals are also observed, suggesting the presence of trace terminal aldehyde defects that are commonly encountered in interfacially polymerized COF membranes. In contrast, COF-3CO exhibits negligible C═N vibration but shows absorption bands at 1572 cm^{-1} and 1289 cm^{-1}, assignable to C═C and C–N stretching modes, indicative of predominant enol-keto tautomerization and formation of β-ketoamine linkages (Figures S1–S4) [56]. Consistently, solid-state ^{13}C NMR spectra show a carbonyl (C═O) resonance at 185.3 ppm for COF-3CO [57–59], whereas the other membranes display imine carbon signals at ~162.0 ppm (Figures S5–S8). Powder x-ray diffraction (PXRD) confirms long-range crystallinity (Figure S9), and N_2 sorption isotherms demonstrate permanent porosity. Brunauer–Emmett–Teller (BET) surface areas are 847, 854, 708, and 1058 m^2 g^{-1} for COF-0OH, COF-1OH, COF-2OH, and COF-3CO, respectively, with narrow pore-size distributions centered at 0.54, 0.51, 0.49, and 0.51 nm (Figures S10 and S11). The comparable pore dimensions ensure similar mass-transport characteristics across the series, isolating hydroxyl functionality as the primary variable controlling catalytic behavior. Water contact angle measurements show that all COF membranes exhibit comparable surface hydrophobicity, with water contact angles (WCA) around 100°, regardless of hydroxyl content (Figure S12). This observation suggests that the hydroxyl groups are preferentially oriented toward the internal pore channels rather than exposed on the external membrane surface. This internal localization is critical for preserving favorable gas-solid interfaces for O_2 adsorption while establishing proton-accessible nanochannels essential for coordinated PCET.

2.2 | Photocatalytic Performance Evaluation of COF Membranes

With the membrane structures and pore-wall chemistries established, the photocatalytic performance of the COF membranes was evaluated for H_2O_2 production in pure water under ambient conditions. All reactions were carried out without sacrificial agents or cocatalysts under simulated one-sun irradiation from a Xe lamp (100 mW cm^{-2}). Circular COF membranes with a diameter of 2 cm were directly used as photocatalysts (Figure 3a). Owing to their intrinsic hydrophobicity, the membranes spontaneously floated at the air-water interface, forming a stable gas-liquid-solid triphase configuration. This interfacial arrangement ensures continuous O_2 access while maintaining a confined membrane environment for coupled proton and electron transport during photocatalysis [60–63].

Under identical conditions, the H_2O_2 production rate shows a strong dependence on the hydroxyl functionality within the COF channels. The hydroxyl-free COF-0OH membrane exhibits a relatively low production rate of 1.25 mmol g^{-1} h^{-1}. Introducing one hydroxyl group markedly increases the rate to 11.31 mmol g^{-1} h^{-1} for COF-1OH, while further increasing the hydroxyl density gives the highest activity for COF-2OH, reaching 21.79 mmol g^{-1} h^{-1}. In contrast, COF-3CO, in which the phenolic hydroxyl groups are largely consumed through enol-keto tautomerization to form β-ketoenamine linkages, delivers a much lower rate of 1.96 mmol g^{-1} h^{-1}. This non-monotonic activity trend indicates that free phenolic hydroxyl groups, rather than hydroxyl incorporation alone, are critical for promoting H_2O_2 generation. The optimized activity of COF-2OH suggests that an appropriate density of accessible hydroxyl groups can create a balanced proton-management environment for coordinated PCET.

The importance of O_2 availability was further examined by switching the reaction atmosphere from ambient air to pure O_2.

15214095, 2026, 46, Downloaded from https://advanced.onlinelibrary.wiley.com/doi/10.1002/adma.73980 by Shengqian Ma - University Of North Texas Willis Library , Wiley Online Library on [21/10/2026]. See the Terms and Conditions (https://onlinelibrary.wiley.com/terms-and-conditions) on Wiley Online Library for rules of use; OA articles are governed by the applicable Creative Commons License

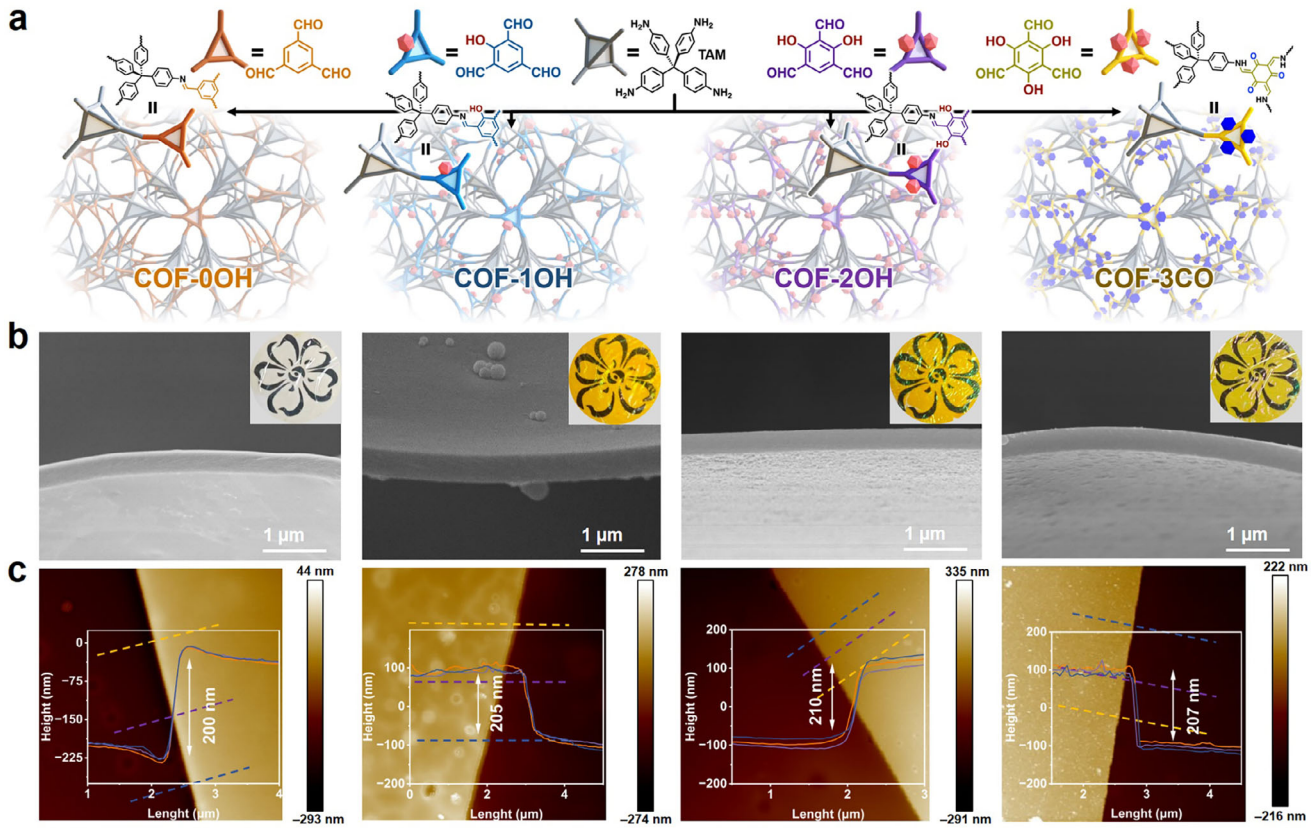


FIGURE 2 | Membrane synthesis and structural characterization of COF membranes. (a) Synthetic scheme illustrating the chemical structures of the COF membranes and their cubic crystal lattice (space group I-43d). (b) SEM images of COF-0OH, COF-1OH, COF-2OH, and COF-3CO membranes (from left to right); inset: photographs of the corresponding free-standing membranes transferred onto photographic paper. (c) AFM images of COF-0OH, COF-1OH, COF-2OH, and COF-3CO membranes (from left to right), with insets showing the corresponding height profiles along the indicated scan lines.

Under O_2-saturated conditions, the H_2O_2 production rate of COF-2OH increases from 21.79 to 26.40 mmol g^{-1} h^{-1}, corresponding to a 21.2% enhancement (Figure 3b). This result confirms that molecular O_2 is a key reactant in the photocatalytic process, while the moderate increase also suggests that the membrane-confined reaction environment already provides efficient O_2 access under ambient air. Under sacrificial-agent-free and one-sun irradiation conditions, the H_2O_2 production rate of COF-2OH ranks among the highest values reported for COF-based photocatalysts (Figure 3c; Table S1). The membrane also shows good operational stability. Post-reaction FT-IR spectra of COF-2OH remain nearly identical to those of the fresh membrane, with no obvious changes in the characteristic vibrational bands. Recycling experiments further show that the H_2O_2 production rate is well retained, confirming the structural robustness and catalytic durability of the hydroxyl-containing COF membrane under photocatalytic conditions (Figure S13).

Because weak residual carbonyl signals were observed in the FT-IR spectra of the imine-linked COF membranes, we further examined whether trace aldehyde defects could contribute to the measured photocatalytic activity. Benzaldehyde was introduced as a molecular aldehyde control, with the added amount conservatively estimated as 2.5 μg by assuming that all possible residual aldehyde groups in the membrane remained unreacted. After benzaldehyde addition, the H_2O_2 production rate of COF-2OH increases only slightly from 21.79 to 23.93 mmol g^{-1} h^{-1} (Figure S14). This limited enhancement indicates that residual aldehyde species may contribute marginally, but they are not the dominant origin of the high H_2O_2 production activity.

To distinguish the role of membrane architecture from that of chemical composition alone, the chemically identical dihydroxylated COF was further tested in powder form and as a pressed self-supporting pellet under otherwise identical conditions. The COF-2OH powder shows a drastically reduced H_2O_2 production rate of only 0.33 mmol g^{-1} h^{-1}, more than 60-fold lower than that of the membrane (Figure 3b). The powder also exhibits a much lower apparent WCA of approximately 47°, compared with approximately 108° for the membrane (Figure S15), which is attributed to its particulate morphology and interparticle capillary water uptake. Consequently, the powder rapidly sinks into the aqueous phase during photocatalysis, whereas the membrane remains floating at the air-water interface and maintains a stable triphase configuration.

To further isolate the effect of flotation, COF-2OH powder was compressed into a self-supporting pellet capable of floating on the water surface. However, the floating pellet shows even lower activity than the immersed powder, with almost no detectable H_2O_2 production (Figure S16). This result demonstrates that flotation alone is insufficient to reproduce the exceptional

15214095, 2026, 46, Downloaded from https://advanced.onlinelibrary.wiley.com/doi/10.1002/adma.73980 by Shengqian Ma - University Of North Texas Willis Library , Wiley Online Library on [21/10/2026]. See the Terms and Conditions (https://onlinelibrary.wiley.com/terms-and-conditions) on Wiley Online Library for rules of use; OA articles are governed by the applicable Creative Commons License

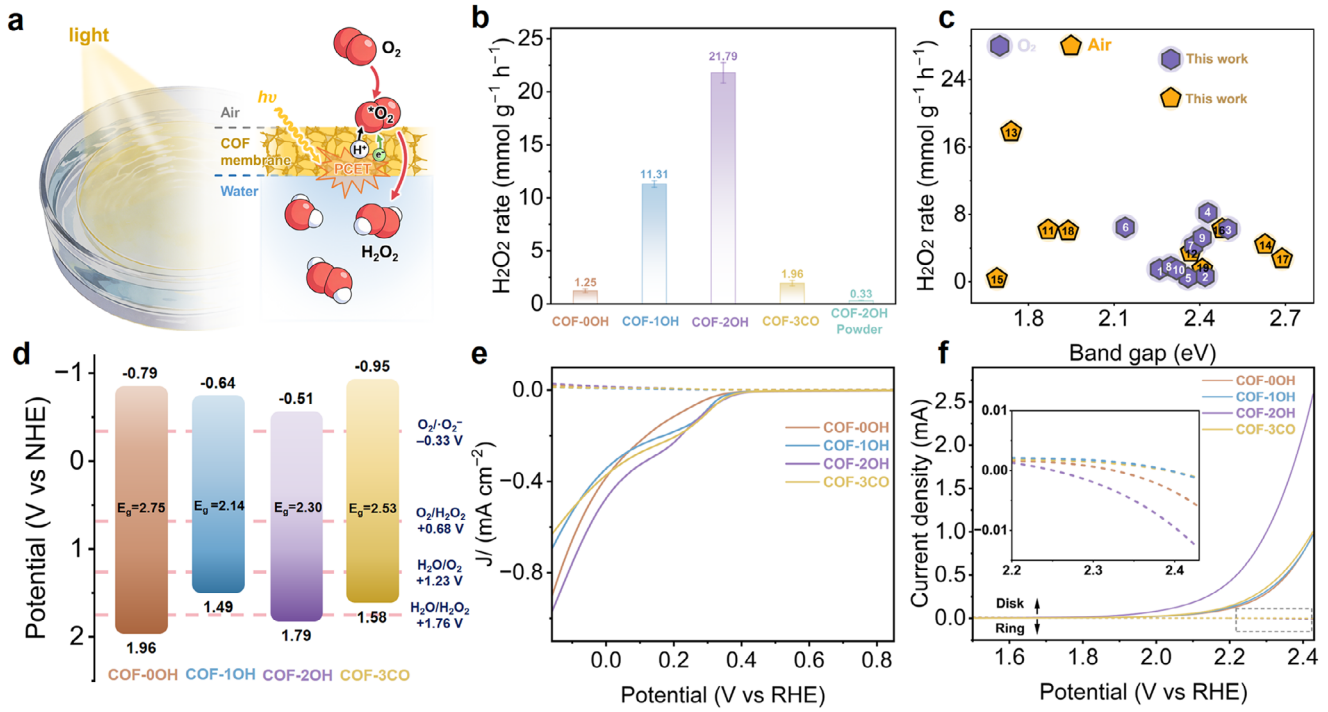


FIGURE 3 | (a) Schematic illustration of membrane-based photocatalytic H_2O_2 synthesis from H_2O and O_2. (b) Comparison of H_2O_2 production rates for different catalytic systems after 1 h of irradiation under a Xe lamp (100 mW cm^{-2}) in ambient air. Error bars represent the standard deviation from three independent measurements. (c) Benchmark comparison of the COF-2OH membrane with previously reported COF-based photocatalysts under Xe lamp irradiation (100 mW cm^{-2}); entry numbers correspond to the systems listed in Table S1. (d) Experimentally determined electronic band structures of the COF membranes. (e) Linear sweep voltammetry recorded using a RRDE for COF-0OH, COF-1OH, COF-2OH, and COF-3CO. (f) Corresponding RRDE voltammograms measured in 0.1 M phosphate buffer solution at a scan rate of 10 mV s^{-1} and a rotation rate of 1600 rpm; the Pt ring electrode was held at 0.6 V versus Ag/AgCl for H_2O_2 detection.

performance of the COF-2OH membrane. The pressed pellet should be regarded as a macroscopically shaped form of compressed COF powder rather than a continuous COF membrane; microscopically, it still consists of packed COF particles with interparticle boundaries and discontinuous transport pathways. Therefore, the poor activity of the pellet is likely caused by particle compaction, which reduces accessible surface area, blocks pore and interparticle diffusion pathways, limits light penetration, and weakens reactant accessibility. These control experiments confirm that the superior activity of the COF-2OH membrane arises from the cooperative integration of a stable triphase interface, efficient O_2 accessibility, continuous thin-film charge transport, and hydroxyl-regulated proton management within ordered nanochannels. These features establish a membrane-confined environment that enables more coordinated proton/electron transfer and accounts for the markedly enhanced photocatalytic H_2O_2 production.

2.3 | Optical and Electrochemical Properties

To clarify whether the differences in photocatalytic activity arise primarily from light absorption or electronic structure, the optical and electrochemical properties of the COF membranes were systematically investigated. UV–vis absorption spectra show that hydroxyl substitution markedly affects the visible-light absorption profiles of the membranes, in agreement with their distinct color changes. Tauc plot analysis gives optical band gaps of 2.75, 2.13, 2.30, and 2.53 eV for COF-0OH, COF-1OH, COF-2OH and COF-3CO, respectively (Figure S17). Notably, COF-1OH exhibits a narrower band gap than COF-2OH but shows much lower H_2O_2 production activity. This non-monotonic relationship indicates that light absorption alone cannot account for the observed catalytic trend. Instead, charge separation, proton/electron transport, and the local pore microenvironment must also play decisive roles in determining photocatalytic performance.

Mott–Schottky measurements were then used to determine the band positions of the COF membranes. The conduction band minimum (CBM) potentials are estimated to be −0.79, −0.64, −0.51, and −0.95 eV for COF-0OH, COF-1OH, COF-2OH and COF-3CO, respectively, all of which are more negative than the thermodynamic potential required for two-electron oxygen reduction to H_2O_2. These results confirm that photocatalytic H_2O_2 formation through O_2 reduction is energetically feasible for all membranes. Combined with their optical band gaps, the corresponding valence band maximum (VBM) potentials are calculated to be 1.96, 1.49, 1.79, and 1.58 eV, respectively (Figure 3d; Figure S18). Among them, COF-0OH and COF-2OH possess sufficiently positive valence-band potentials to support oxidative half-reactions involving water, suggesting that water may also participate in the overall photocatalytic cycle. For COF-2OH in particular, this band alignment is consistent with the involvement of water-related oxidative processes, which can provide charge-compensating hole consumption during continuous O_2 reduction in the sacrificial-agent-free photocatalytic system.

15214095, 2026, 46, Downloaded from https://advanced.onlinelibrary.wiley.com/doi/10.1002/adma.73980 by Shengqian Ma - University Of North Texas Willis Library , Wiley Online Library on [21/10/2026]. See the Terms and Conditions (https://onlinelibrary.wiley.com/terms-and-conditions) on Wiley Online Library for rules of use; OA articles are governed by the applicable Creative Commons License

Rotating ring-disk electrode (RRDE) measurements further support the oxygen-reduction activity of the membranes. All COF membranes show electrochemical responses associated with H_2O_2 generation through the oxygen reduction reaction, while COF-2OH displays the highest disk and ring currents, indicating more favorable reaction kinetics toward H_2O_2 formation (Figure 3e,f, and Figure S19). To examine whether H_2O_2 generation relies exclusively on externally supplied O_2, photocatalytic experiments were further performed under an N_2 atmosphere. The COF-2OH membrane still produces H_2O_2 at a rate of 4.72 mmol g^{-1} h^{-1}, although this value is much lower than that obtained under air. This result suggests that water-derived species may contribute to H_2O_2 formation under O_2-limited conditions.

To verify the possible involvement of water in H_2O_2 generation, an $H_2{}^{18}O$ isotope-labeling experiment was carried out using the COF-2OH membrane, followed by GC–MS analysis of the decomposed H_2O_2 products (Figure S20). The detection of isotope-labeled oxygen species confirms that water-derived species can participate in H_2O_2 formation under photocatalytic conditions. Together with the much higher H_2O_2 production rate observed under air than under N_2, these results indicate that molecular O_2 serves as the dominant oxygen source for H_2O_2 accumulation, while water participates in the accompanying oxidative and proton-transfer processes. Accordingly, two-electron O_2 reduction is coupled with water-involving oxidative charge compensation, which consumes photogenerated holes, maintains charge neutrality, and replenishes local protons within the membrane-confined PCET environment.

Additional inhibitor experiments further support this coupled redox picture. The introduction of $AgNO_3$ as an electron scavenger or operation under N_2 atmosphere markedly suppresses H_2O_2 production, confirming the essential role of photogenerated electrons and O_2 reduction. In contrast, when $AgNO_3$, EDTA-2Na, and N_2 are introduced simultaneously, H_2O_2 generation is almost completely inhibited (Figure S21), indicating that both photogenerated electrons and holes are required to sustain the overall catalytic cycle.

Because COF-3CO predominantly undergoes enol-keto tautomerization and contains β-ketoenamine linkages rather than free phenolic hydroxyl groups, its linkage chemistry differs from that of the imine-linked COF-0OH, COF-1OH, and COF-2OH membranes. Therefore, the subsequent mechanistic analysis focuses on COF-0OH, COF-1OH, and COF-2OH to elucidate the intrinsic role of free hydroxyl groups in regulating PCET. Density functional theory (DFT) calculations were first performed to examine how hydroxyl substitution modulates electronic polarization within the COF framework. The calculated dipole moments (μ) of representative COF fragments increase with hydroxyl density, indicating that phenolic –OH groups introduce stronger local polarization into the pore walls. Such polarization can facilitate charge separation and directional carrier migration by creating a more asymmetric electronic environment within the framework [64–66]. Time-dependent DFT calculations (TD-DFT) further show that the $S_0 \rightarrow S_1$ excitation energy and ionization energy (IE) decrease in the order COF-0OH > COF-1OH > COF-2OH, suggesting that hydroxyl-functionalized COFs are more readily photoexcited [25, 67].

The electron-hole separation behavior was further analyzed using the electron-hole overlap index. The overlap index decreases from COF-0OH to COF-2OH, indicating progressively reduced spatial overlap between photogenerated electrons and holes (Sr, Figure 4a; Figures S22–S24) [68, 69]. Although COF-2OH shows a relatively high exciton binding energy (E_b), the reduced electron-hole overlap suggests that hydroxyl-induced polarization and the ordered membrane framework help suppress recombination and promote charge separation. This interpretation is consistent with the experimental photoelectrochemical results. Transient photocurrent responses follow the order COF-2OH > COF-1OH > COF-0OH, while electrochemical impedance spectroscopy (EIS) shows the opposite trend in charge-transfer resistance (Figure 4b,c) [70]. These theoretical and experimental results demonstrate that COF-2OH provides the most favorable electronic environment for photogenerated charge separation and transport, which is essential for sustaining efficient PCET during photocatalytic H_2O_2 synthesis.

To clarify how hydroxyl substitution affects the elementary steps of H_2O_2 formation, we first examined O_2 adsorption on representative imine-linked COF segments. Electrostatic potential (ESP) mapping shows that the introduction of phenolic hydroxyl groups markedly redistributes the local electrostatic environment of the pore walls, generating more polarized regions that are favorable for O_2 binding and activation (Figures S25–S27). After screening possible adsorption configurations, the most stable O_2-bound states show increasingly negative adsorption energies in the order COF-0OH, COF-1OH, and COF-2OH (Figure 5a), indicating progressively strengthened O_2 adsorption with increasing hydroxyl density. These results suggest that hydroxyl groups facilitate O_2 activation, although the adsorption energy should be regarded as a qualitative descriptor rather than a direct predictor of the overall H_2O_2 production rate. The photocatalytic activity is ultimately governed by the combined effects of O_2 adsorption, intermediate stabilization, local proton availability, and membrane-facilitated charge transport.

Electrochemical and radical-trapping experiments further confirm the involvement of the two-electron oxygen reduction pathway. RRDE measurements give average electron-transfer numbers close to 2.0 for COF-0OH, COF-1OH, and COF-2OH, confirming that H_2O_2 formation predominantly proceeds through a $2e^-$ ORR pathway (Figure 5b). Consistently, the addition of *p*-benzoquinone (*p*-BQ), a superoxide ($\bullet O_2^-$) scavenger, suppresses the H_2O_2 production rate of COF-2OH by 71.6%, indicating that $\bullet O_2^-$ is a key intermediate in the reaction pathway [71–74]. To directly detect this intermediate, EPR measurements were performed using BMPO as the spin-trapping agent under identical photocatalytic conditions. The COF-2OH membrane shows a much stronger BMPO–$\bullet O_2^-$ adduct signal than the corresponding powder catalyst (Figure S28), demonstrating that the membrane configuration promotes O_2 activation and enhances the generation of superoxide intermediates.

Free-energy calculations along the $2e^-$ ORR pathway further reveal the role of hydroxyl groups in stabilizing reaction intermediates. Hydroxyl incorporation stabilizes both adsorbed O_2 and the *OOH intermediate, with COF-2OH showing the lowest free-energy barrier for *OOH formation, which is identified as the rate-determining step (Figure 5c). This reduced barrier can be

15214095, 2026, 46, Downloaded from https://advanced.onlinelibrary.wiley.com/doi/10.1002/adma.73980 by Shengqian Ma - University Of North Texas Willis Library , Wiley Online Library on [21/10/2026]. See the Terms and Conditions (https://onlinelibrary.wiley.com/terms-and-conditions) on Wiley Online Library for rules of use; OA articles are governed by the applicable Creative Commons License

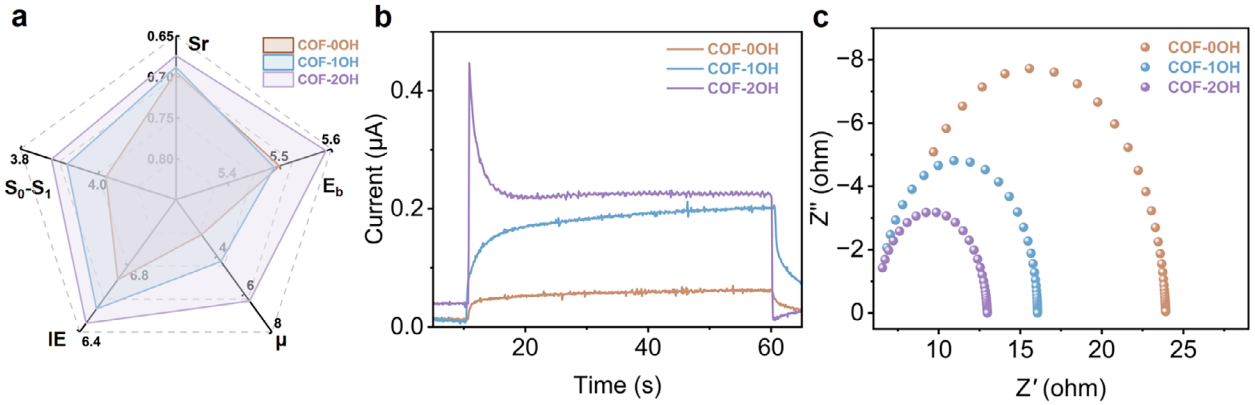


FIGURE 4 | (a) Radar plot comparing the COF membranes in terms of their propensity for photogenerated electron-hole separation and recombination. (b) Transient photocurrent responses of the COF membranes measured in 0.1 M Na_2SO_4 under Xe lamp irradiation (100 mW cm^{-2}). (c) EIS Nyquist plots recorded in 0.1 M Na_2SO_4 over a frequency range of 21 Hz to 100 kHz.

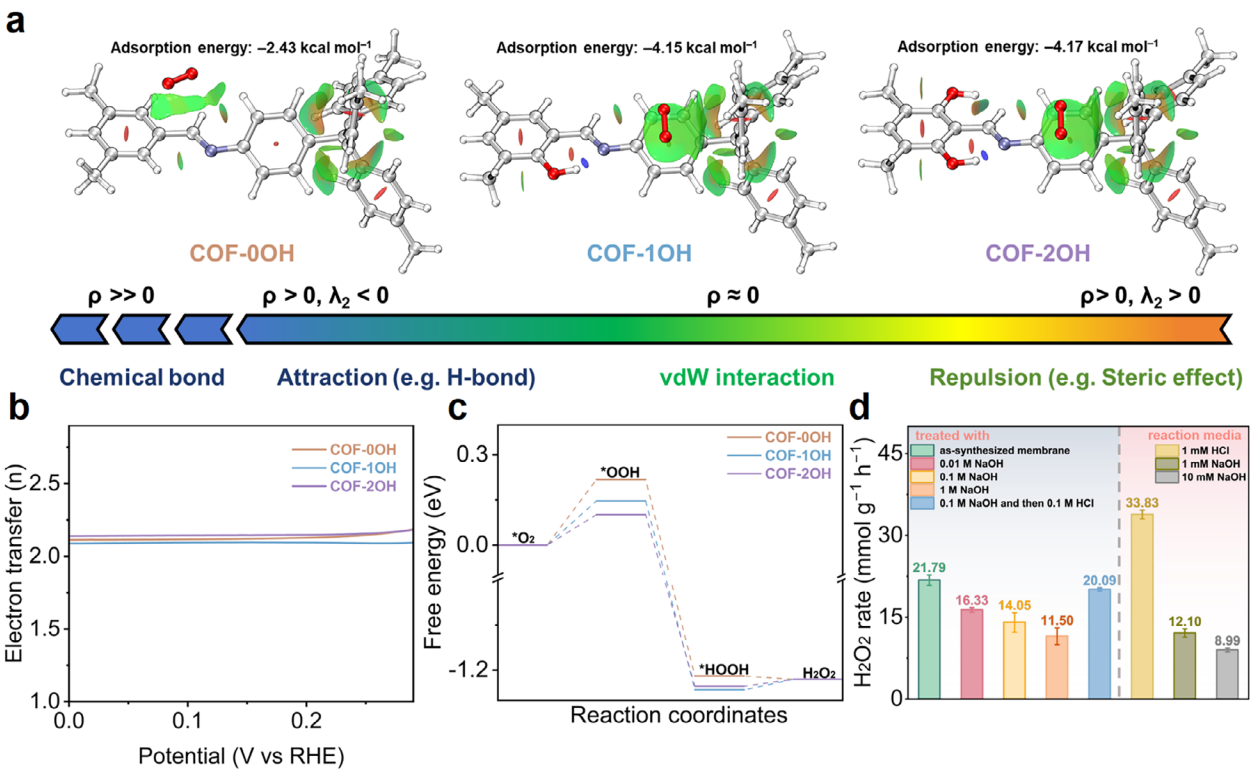


FIGURE 5 | (a) Interaction region indicator (IRI) analysis of weak interactions between adsorbed O_2 and representative segments of the COF-0OH, COF-1OH, and COF-2OH membranes. Green regions correspond to van der Waals interactions, brown/red regions indicate steric repulsion, and blue regions represent hydrogen bonding. Here, ρ denotes the electron density, and λ_2 is the second largest eigenvalue of the Hessian matrix of ρ. (b) Average electron transfer number (n) of COF-0OH, COF-1OH, and COF-2OH during the ORR. (c) Gibbs free-energy diagrams of the ORR pathways on respresentive segments of the COF-0OH, COF-1OH, and COF-2OH membranes. (d) Comparison of H_2O_2 production rates of the COF-2OH membrane before and after treatment under different conditions, as well as its catalytic performance in various reaction media. All reactions were conducted under Xe lamp irradiation (100 mW cm^{-2}) using 2 mL of solvent and a single membrane (diameter: 2 cm).

attributed to the locally enriched and dynamically available protons provided by phenolic hydroxyl groups within the confined nanochannels. Therefore, the hydroxyl groups do not merely modify O_2 adsorption; more importantly, they participate in regulating the proton supply required for the PCET step leading to *OOH formation.

The functional importance of free phenolic hydroxyl groups was further verified by controlled deprotonation of COF-2OH using NaOH treatment. Progressive conversion of –OH into –ONa was supported by increasing Na incorporation as the NaOH concentration increased, reaching Na contents of 14.1%, 15.5%, and 29.0% for membranes treated with 0.01, 0.1, and 1 M

15214095, 2026, 46, Downloaded from https://advanced.onlinelibrary.wiley.com/doi/10.1002/adma.73980 by Shengqian Ma - University Of North Texas Willis Library , Wiley Online Library on [21/10/2026]. See the Terms and Conditions (https://onlinelibrary.wiley.com/terms-and-conditions) on Wiley Online Library for rules of use; OA articles are governed by the applicable Creative Commons License

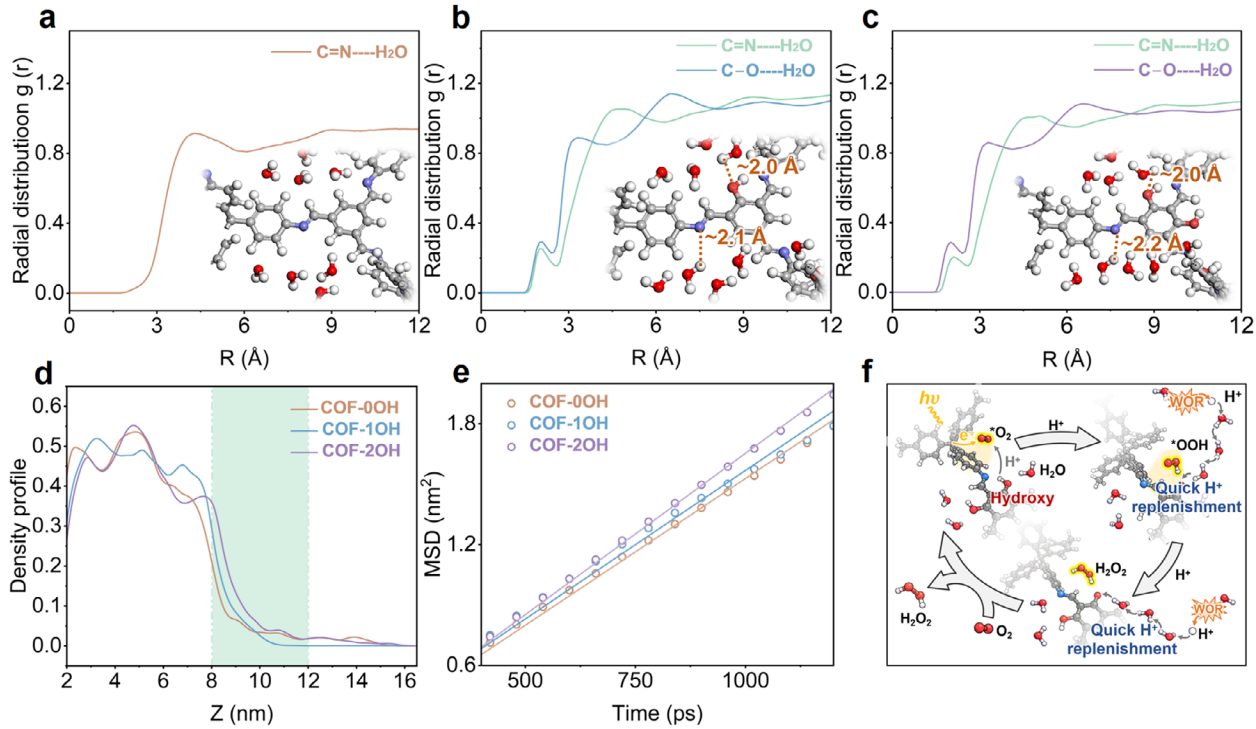


FIGURE 6 | RDF between H_2O molecules and O or N atoms in (a) COF-0OH, (b) COF-1OH, and (c) COF-2OH. (d) Proton density profiles along the z-axis within the COF membranes, with the gray-green shaded regions indicating the membrane boundaries. (e) MSD analysis of protons that transport through the COF-0OH, COF-1OH and COF-2OH membrane. (f) Schematic illustration of the synergistic regulation of proton accumulation, transport, and recycling, forming a dynamic proton-recycling loop that sustains continuous and highly efficient photocatalytic H_2O_2 production in the COF-2OH membrane (atom colors: N, blue; O, red; C, grey; H, white).

NaOH, respectively. Correspondingly, the H_2O_2 production rate decreases from 21.79 mmol g^{-1} h^{-1} for pristine COF-2OH to 16.33, 14.05 and 11.50 mmol g^{-1} h^{-1} after treatment with 0.01, 0.1, and 1 M NaOH, respectively. This activity decline demonstrates that free phenolic hydroxyl groups are essential for maintaining efficient proton transfer within the nanochannels. Importantly, subsequent treatment with 0.1 M HCl restores the activity to 20.09 mmol g^{-1} h^{-1}, confirming that the activity loss is largely reversible and is associated with hydroxyl deprotonation rather than irreversible structural degradation. The proton-reservoir function of the hydroxyl groups was further examined under different solution conditions. When the reaction is conducted in 1 mM HCl, the H_2O_2 production rate increases from 21.79 to 33.8 mmol g^{-1} h^{-1}, consistent with enhanced proton availability. In contrast, operation in 1 mM NaOH lowers the activity to 12.10 mmol g^{-1} h^{-1}, while increasing the NaOH concentration to 10 mM further decreases the rate to 8.99 mmol g^{-1} h^{-1} (Figure 5d).

To further understand proton transport within the COF nanochannels, molecular dynamics (MD) simulations were performed. Trajectory analysis reveals a clear dependence of proton mobility on hydroxyl density, with proton transport becoming more efficient as more phenolic hydroxyl groups are incorporated into the channel walls. Radial distribution function (RDF) analysis shows pronounced hydrogen-bonding correlations at 2–3 Å between water molecules and both phenolic –OH and imine C═N sites in hydroxyl-functionalized COFs, indicating the formation of continuous hydrogen-bonded networks that facilitate proton transfer (Figure 6a–c). In contrast, COF-0OH shows much weaker water-framework interactions, consistent with its poor proton-transport capability. Beyond promoting proton mobility, hydroxyl groups also enrich protons within the confined nanochannels. Strong hydrogen bonding between phenolic –OH groups and surrounding water molecules creates an interfacial water layer that retains protons near the catalytic sites, forming a local proton-rich microenvironment favorable for PCET. Proton density profiles follow the order COF-2OH > COF-1OH > COF-0OH, confirming that higher hydroxyl density leads to stronger proton accumulation within the membrane channels (Figure 6d). Consistently, mean-square displacement (MSD) analysis and trajectory snapshots show faster proton diffusion in COF-2OH than in COF-1OH and COF-0OH (Figure 6e; Figures S29–S31). These results demonstrate that COF-2OH simultaneously provides high local proton concentration and efficient proton mobility. This dual function enables rapid proton delivery to O_2-derived intermediates and replenishment of protons during continuous photocatalysis, thereby establishing a dynamic proton-recycling loop that sustains efficient membrane-confined PCET and high-rate H_2O_2 production (Figure 6f).

2.4 | Construction of Membrane Reactor for Organic Pollutant Degradation

To assess the operational robustness and practical applicability of the membrane-enabled PCET system under conditions relevant to real-world water treatment, we first evaluated the H_2O_2 generation performance of the COF-2OH membrane under varying illumination intensities. As expected, the H_2O_2 production rate

15214095, 2026, 46, Downloaded from https://advanced.onlinelibrary.wiley.com/doi/10.1002/adma.73980 by Shengqian Ma - University Of North Texas Willis Library , Wiley Online Library on [21/10/2026]. See the Terms and Conditions (https://onlinelibrary.wiley.com/terms-and-conditions) on Wiley Online Library for rules of use; OA articles are governed by the applicable Creative Commons License

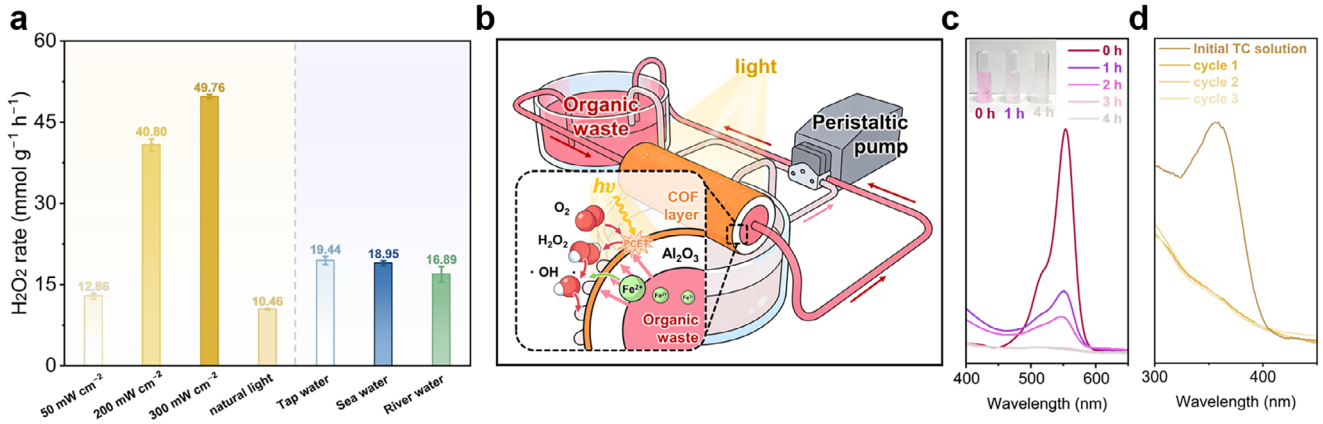


FIGURE 7 | (a) H_2O_2 production rates catalyzed by the COF-2OH membrane under different illumination intensities, water sources, and reaction atmospheres. Tap water was collected from municipal pipelines, seawater from the Yellow Sea, and river water from the Yuhangtang River at the Zijingang Campus of Zhejiang University. (b) Schematic illustration of the integration of the COF-2OH membrane with a tubular Al_2O_3 support for continuous degradation of organic pollutants using in situ-generated H_2O_2. (c) Time-dependent evolution of RhB concentration monitored by UV–vis spectroscopy. The experiments were conducted by degrading 100 mL of a mixed solution containing RhB (2 mg L^{-1}) and $FeSO_4{\cdot}7H_2O$ (10 mg L^{-1}) under Xe lamp irradiation (100 mW cm^{-2}), using the composite membrane with an effective COF membrane area of 15 cm^2 as the photocatalyst. (d) Time-dependent evolution of TC concentration monitored by UV–vis spectroscopy. The experiments were carried out using 60 mL of a mixed solution containing TC (2 mg L^{-1}) and $FeSO_4{\cdot}7H_2O$ (10 mg L^{-1}) under Xe lamp irradiation (100 mW cm^{-2}) with the same composite membrane configuration. The solution was supplied in three batches of 20 mL at 1 h intervals.

increases monotonically with light intensity, reaching 49.76 mmol g^{-1} h^{-1} at 300 mW cm^{-2}, approximately 2.3 times higher than that obtained under one-sun irradiation (100 mW cm^{-2}). Notably, under natural sunlight with an average irradiance of 45.3 mW cm^{-2}, the membrane maintains a stable H_2O_2 production rate of 10.46 mmol g^{-1} h^{-1}, underscoring its robustness under realistic illumination conditions.

The environmental tolerance of the membrane-enabled PCET process was further examined in various natural water matrices, including river water, seawater, and tap water. In all cases, the COF-2OH membrane retains 75–90% of the H_2O_2 production efficiency observed in deionized water, indicating strong resistance to interference from complex ionic compositions and dissolved organic matter.

Building on its robust and tunable H_2O_2 generation capability, the COF-2OH membrane was further integrated into a catalytic membrane reactor to enable the in situ utilization of photocatalytically generated H_2O_2 through advanced oxidation processes. Specifically, $FeSO_4{\cdot}7H_2O$ was introduced to initiate the photo-Fenton reaction ($H_2O_2 + Fe^{2+} \rightarrow Fe^{3+} + OH^- + {\bullet}OH$), thereby producing highly reactive hydroxyl radicals for the degradation of persistent organic pollutants. Benefiting from their free-standing nature and mechanical flexibility, the COF membranes can be readily incorporated into continuous-flow reactor configurations. As a proof-of-concept, a tubular aluminum oxide (Al_2O_3) support was employed to construct a composite membrane reactor, in which the COF-2OH membrane was immobilized on the outer surface of the tube while the pollutant-containing solution was continuously circulated through the inner channel (Figure 7b). This configuration enables continuous O_2 access at the membrane-air interface while maintaining intimate contact between the aqueous phase and catalytic surface, thereby facilitating efficient interfacial mass transfer and sustained photo-Fenton reactions under continuous-flow operation.

Rhodamine B (RhB) and tetracycline (TC) were selected as representative dyes and pharmaceutical contaminants to evaluate the oxidative performance of the reactor. Under photo-Fenton conditions in the presence of Fe^{2+}, the membrane reactor exhibits rapid and highly efficient pollutant degradation. At an initial concentration (C_0) of 2 mg L^{-1}, 99.4% of RhB in 100 mL solution is removed within 4 h (Figure 7c), while complete degradation of 20 mL TC solution (2 mg L^{-1}) is achieved within 1 h. Baseline fluctuations observed in the UV–vis spectra are attributed to dissolved iron species (Figure S32). To distinguish genuine photocatalytic/photo-Fenton degradation from possible adsorption effects, dark adsorption control experiments were performed using the identical COF-2OH/Al_2O_3 membrane-reactor system in the absence of light. Under dark conditions, RhB removal reaches only 14.5% after 3 h (Figures S33 and S34), indicating that adsorption on the membrane/support contributes only modestly to the initial concentration decrease. Such adsorption may facilitate subsequent degradation by locally enriching pollutant molecules near the catalytic membrane surface and enhancing their interaction with in situ-generated H_2O_2 and reactive oxygen species. However, this contribution is clearly minor compared with the photocatalytic/photo-Fenton process under irradiation. These results confirm that the dominant contribution to pollutant removal arises from genuine oxidative degradation rather than passive adsorption alone. More importantly, the degradation efficiency is well maintained over at least three consecutive cycles (Figure 7d), demonstrating the operational stability and reusability of the membrane reactor. These results demonstrate that membrane-enabled, PCET-regulated H_2O_2 generation can be directly coupled with downstream oxidation chemistry in a single integrated platform, highlighting its strong potential for practical and scalable water-treatment applications.

15214095, 2026, 46, Downloaded from https://advanced.onlinelibrary.wiley.com/doi/10.1002/adma.73980 by Shengqian Ma - University Of North Texas Willis Library , Wiley Online Library on [21/10/2026]. See the Terms and Conditions (https://onlinelibrary.wiley.com/terms-and-conditions) on Wiley Online Library for rules of use; OA articles are governed by the applicable Creative Commons License

3 | Conclusion

In summary, this work demonstrates that molecularly engineered COF membranes provide an effective platform for regulating proton-coupled electron transfer in heterogeneous photocatalysis. By constructing a series of 3D COF membranes with systematically varied phenolic hydroxyl densities, we show that ordered membrane nanochannels can serve not only as photoactive frameworks but also as confined proton-management environments. The incorporated hydroxyl groups modulate local proton availability, O_2 adsorption, charge separation, and intermediate stabilization, thereby enabling a closer match between proton supply and photogenerated electron transport during photocatalytic H_2O_2 synthesis. Among the membranes studied, COF-2OH offers the most favorable balance between accessible proton reservoirs and efficient charge transport. The spatially confined phenolic hydroxyl groups promote O_2 activation, lower the barrier for *OOH formation, and support proton accumulation and transport within the nanochannels. As a result, COF-2OH achieves an H_2O_2 production rate of 21.79 mmol g^{-1} h^{-1} under one-sun irradiation in pure water without sacrificial agents or cocatalysts, far exceeding the corresponding powder catalyst. Control experiments using powder and pellet catalysts further indicate that the high activity arises from the cooperative effect of pore-wall chemistry, continuous thin-film architecture, stable gas-liquid-solid interfacial contact, and membrane-confined proton/electron transport. The COF-2OH membrane also maintains good activity under natural sunlight and in complex water matrices, highlighting the robustness of the membrane-enabled photocatalytic process. Moreover, its free-standing and interfacially accessible structure allows direct integration into a tubular Al_2O_3-supported membrane reactor, where in situ-generated H_2O_2 can be coupled with photo-Fenton chemistry for efficient degradation of organic pollutants. This proof-of-concept demonstration suggests that proton-managing COF membranes may offer a useful route for connecting solar-driven H_2O_2 production with downstream environmental applications. Overall, these findings provide design insights into how ordered membrane nanochannels can be used to regulate local proton environments and improve PCET efficiency. More broadly, this work highlights the potential of COF membranes as programmable reaction interfaces for solar-to-chemical conversion, selective oxygen reduction, and integrated photocatalytic water-treatment systems.

Acknowledgements

This work was supported by the National Key Research and Development Program of China (No. 2022YFA1503004) and the National Science Foundation of China (Nos. 22421004 and 22125204). The authors appreciate the assistance of Fang Chen from the Analytical Testing Center of the Department of Chemistry, Zhejiang University, in conducting SEM measurements.

Conflicts of Interest

The authors declare no conflicts of interest.

Data Availability Statement

The data that support the findings of this study are available in the supplementary material of this article.

References

1. S. Hammes-Schiffer, "Exploring Proton-Coupled Electron Transfer at Multiple Scales," *Nature Computational Science* 3 (2023): 291–300, https://doi.org/10.1038/s43588-023-00422-5.

2. Y. Hao, Y. Kang, S. Wang, et al., "Electrode/Electrolyte Synergy for Concerted Promotion of Electron and Proton Transfers toward Efficient Neutral Water Oxidation," *Angewandte Chemie International Edition* 62 (2023): 202303200, https://doi.org/10.1002/anie.202303200.

3. W. D. Guerra, E. Odella, M. Secor, et al., "Role of Intact Hydrogen-Bond Networks in Multiproton-Coupled Electron Transfer," *Journal of the American Chemical Society* 142 (2020): 21842–21851, https://doi.org/10.1021/jacs.0c10474.

4. T. Wang, Y. Zhang, B. Huang, et al., "Enhancing Oxygen Reduction Electrocatalysis by Tuning Interfacial Hydrogen Bonds," *Nature Catalysis* 4 (2021): 753–762, https://doi.org/10.1038/s41929-021-00668-0.

5. A. K. Bains, A. Sau, B. S. Portela, et al., "Efficient Super-Reducing Organic Photoredox Catalysis with Proton-Coupled Electron Transfer Mitigated Back Electron Transfer," *Science* 388 (2025): 1294–1300, https://doi.org/10.1126/science.adw1648.

6. P. Garrido-Barros, J. Derosa, M. J. Chalkley, and J. C. Peters, "Tandem Electrocatalytic N_2 Fixation via Proton-Coupled Electron Transfer," *Nature* 609 (2022): 71–76, https://doi.org/10.1038/s41586-022-05011-6.

7. E. S. Grape and C. K. Brozek, "Turn-On Conductivity with Proton-Coupled Electron Transport in Metal–Organic Frameworks," *Journal of the American Chemical Society* 147 (2025): 40981–40991, https://doi.org/10.1021/jacs.5c14574.

8. D. G. Nocera, "Proton-Coupled Electron Transfer: the Engine of Energy Conversion and Storage," *Journal of the American Chemical Society* 144 (2022): 1069–1081, https://doi.org/10.1021/jacs.1c10444.

9. C. Liu, X. Liu, B. Chen, et al., "Squaric Acid-Based Zwitterionic Covalent Organic Framework Induces Triple Synergy for Boosted Hydrogen Peroxide Photosynthesis," *Nature Communications* 16 (2025): 8941, https://doi.org/10.1038/s41467-025-63997-9.

10. Z. Xue, B. Zhang, Q. Guo, et al., "Sacrificial-Agent-Triggered Mass Transfer Gating in Covalent Organic Framework for Hydrogen Peroxide Photocatalysis," *Advanced Materials* 37 (2025): 10201, https://doi.org/10.1002/adma.202510201.

11. L. Li, X. Lv, Y. Xue, H. Shao, G. Zheng, and Q. Han, "Custom-Design of Strong Electron/Proton Extractor on COFs for Efficient Photocatalytic H_2O_2 Production," *Angewandte Chemie International Edition* 63 (2024): 202320218.

12. D. Xi, Y. Wu, Y. Li, Z. Yan, R. Y. Liu, and M. J. Aziz, "Electrifying Industrial Hydrogen Peroxide Production via Soft Interfacial Molecular Mediation," *Nature Chemistry* 17 (2025): 1883–1890, https://doi.org/10.1038/s41557-025-01940-7.

13. M. Qiao, X. Zhou, Z. Du, P. Wu, and B. Zong, "Chemical and Engineering Bases for Green H_2O_2 Production and Related Oxidation and Ammoximation of Olefins and Analogues," *National Science Review* 11 (2024): nwae243, https://doi.org/10.1093/nsr/nwae243.

14. Y. Ding, S. Maitra, S. Halder, et al., "Emerging Semiconductors and Metal-Organic-Compounds-Related Photocatalysts for Sustainable Hydrogen Peroxide Production," *Matter* 5 (2022): 2119–2167.

15. Y. J. Zhang, J. S. Tao, Y. Hu, et al., "Metal Oxyhalide-based Heterogeneous Catalytic Water Purification with Ultralow H_2O_2 Consumption O_2 Consumption," *Nature Water* 2 (2024): 770–781, https://doi.org/10.1038/s44221-024-00281-y.

16. S. Zuo, G. Zheng, D. Yang, and J. Wang, "A Natural Oxygen-Harvesting Electrode Enables Aeration-Free Electrochemical Advanced Oxidation for in Situ Water Remediation," *Angewandte Chemie International Edition* 64 (2025): 202513329, https://doi.org/10.1002/anie.202513329.

17. H. Hou, X. Zeng, and X. Zhang, "Production of Hydrogen Peroxide by Photocatalytic Processes," *Angewandte Chemie International Edition* 59 (2020): 17356–17376, https://doi.org/10.1002/anie.201911609.

15214095, 2026, 46, Downloaded from https://advanced.onlinelibrary.wiley.com/doi/10.1002/adma.73980 by Shengqian Ma - University Of North Texas Willis Library , Wiley Online Library on [21/10/2026]. See the Terms and Conditions (https://onlinelibrary.wiley.com/terms-and-conditions) on Wiley Online Library for rules of use; OA articles are governed by the applicable Creative Commons License

18. S. Qu, H. Wu, and Y. H. Ng, "Clean Production of Hydrogen Peroxide: a Heterogeneous Solar-Driven Redox Process," *Advanced Energy Materials* 13 (2023): 2301047, https://doi.org/10.1002/aenm.202301047.

19. B. Mishra, A. Alam, A. Chakraborty, et al., "Covalent Organic Frameworks for Photocatalysis," *Advanced Materials* 37 (2024): 2413118, https://doi.org/10.1002/adma.202413118.

20. Z. Yong and T. Ma, "Solar-to-H_2 O_2 Catalyzed by Covalent Organic Frameworks," *Angewandte Chemie International Edition* 62 (2023): 202308980, https://doi.org/10.1002/anie.202308980.

21. S. Yan, Y. Li, X. Yang, X. Jia, J. Xu, and H. Song, "Photocatalytic H_2 O_2 Generation Reaction with a Benchmark Rate at Air-Liquid-Solid Joint Interfaces," *Advanced Materials* 36 (2024): 2307967, https://doi.org/10.1002/adma.202307967.

22. C. Qiao, W. Xian, Z. Lai, et al., "Covalent Organic Framework Membranes with Asymmetric Wettability for Efficient Photocatalytic H_2O_2 Synthesis," *Angewandte Chemie International Edition* 64 (2025): 202519513, https://doi.org/10.1002/anie.202519513.

23. Y. Chen, R. Liu, Y. Guo, et al., "Hierarchical Assembly of Donor–acceptor Covalent Organic Frameworks for Photosynthesis of Hydrogen Peroxide from Water and Air," *Nature Synthesis* 3 (2024): 998–1010, https://doi.org/10.1038/s44160-024-00542-4.

24. H. Guo, S. Wang, X. Chen, et al., "Engineering a Covalent Organic Framework-Based Type-II Heterojunction for Enhanced Photocatalytic H_2O_2 Synthesis," *Nature Synthesis* 4 (2025): 1610–1620, https://doi.org/10.1038/s44160-025-00880-x.

25. R. Liu, D. Zhao, S. Ji, et al., "Harvesting Singlet and Triplet Excitation Energies in Covalent Organic Frameworks for Highly Efficient Photocatalysis," *Nature Materials* 24 (2025): 1245–1257, https://doi.org/10.1038/s41563-025-02281-z.

26. P. Dong, X. Xu, T. Wu, et al., "Stepwise Protonation of Three-Dimensional Covalent Organic Frameworks for Enhancing Hydrogen Peroxide Photosynthesis," *Angewandte Chemie International Edition* 63 (2024): 202405313, https://doi.org/10.1002/anie.202405313.

27. A. Kong, T. Yang, H. Yan, et al., "Three-Dimensional Bicarbazole-Based Covalent Organic Frameworks as Efficient Yeager-Type Photocatalysts for H_2O_2 Generation in a Two-Phase System," *Journal of the American Chemical Society* 147 (2025): 20855–20864, https://doi.org/10.1021/jacs.5c04447.

28. M. D. Zhang, J. R. Huang, C. P. Liang, X. M. Chen, and P. Q. Liao, "Continuous Electrosynthesis of Pure H_2O_2 Solution with Medical-Grade Concentration by a Conductive Ni-Phthalocyanine-Based Covalent Organic Framework," *Journal of the American Chemical Society* 146 (2024): 31034–31041, https://doi.org/10.1021/jacs.4c10675.

29. W. Zhao, P. Yan, B. Li, et al., "Accelerated Synthesis and Discovery of Covalent Organic Framework Photocatalysts for Hydrogen Peroxide Production," *Journal of the American Chemical Society* 144 (2022): 9902–9909, https://doi.org/10.1021/jacs.2c02666.

30. A. Chakraborty, A. Alam, U. Pal, et al., "Enhancing Photocatalytic Hydrogen Peroxide Generation by Tuning Hydrazone Linkage Density in Covalent Organic Frameworks," *Nature Communications* 16 (2025): 503, https://doi.org/10.1038/s41467-025-55894-y.

31. C. Qin, X. Wu, L. Tang, et al., "Dual Donor-Acceptor Covalent Organic Frameworks for Hydrogen Peroxide Photosynthesis," *Nature Communications* 14 (2023): 5238, https://doi.org/10.1038/s41467-023-40991-7.

32. Z. Xie, X. Chen, W. Wang, et al., "Variation of Chemical Microenvironment of Pores in Hydrazone-Linked Covalent Organic Frameworks for Photosynthesis of H_2 O_2," *Angewandte Chemie International Edition* 63 (2024): 202410179, https://doi.org/10.1002/anie.202410179.

33. A. Rodríguez-Camargo, M. W. Terban, M. Paetsch, et al., "Cyclopalladation of a Covalent Organic Framework for Near-Infrared-Light-Driven Photocatalytic Hydrogen Peroxide Production," *Nature Synthesis* 4 (2025): 710–719, https://doi.org/10.1038/s44160-024-00731-1.

34. P. Das, G. Chakraborty, J. Roeser, S. Vogl, J. Rabeah, and A. Thomas, "Integrating Bifunctionality and Chemical Stability in Covalent Organic Frameworks via One-Pot Multicomponent Reactions for Solar-Driven H_2O_2 Production," *Journal of the American Chemical Society* 145 (2023): 2975–2984, https://doi.org/10.1021/jacs.2c11454.

35. P. Huang, Y. Y. Peng, X. H. Wang, et al., "Charge-Distribution and Microenvironment Dual Regulation of Covalent Organic Frameworks for Enhancing Photocatalytic H_2 O_2 and H_2 Production," *Advanced Materials* 38 (2026): 07849, https://doi.org/10.1002/adma.202507849.

36. J. Tang, Z. Liang, H. Qin, et al., "Large-Area Free-Standing Metalloporphyrin-Based Covalent Organic Framework Films by Liquid-Air Interfacial Polymerization for Oxygen Electrocatalysis," *Angewandte Chemie International Edition* 62 (2023): 202214449, https://doi.org/10.1002/anie.202214449.

37. W. Xian, X. Xu, Y. Ge, et al., "Efficient Light-Driven Ion Pumping for Deep Desalination via the Vertical Gradient Protonation of Covalent Organic Framework Membranes," *Journal of the American Chemical Society* 146 (2024): 33973–33982, https://doi.org/10.1021/jacs.4c12829.

38. S. Zhang, J. Chen, W. Chen, et al., "Regulating Water Molecules via Bioinspired Covalent Organic Framework Membranes for Zn Metal Anodes," *Angewandte Chemie International Edition* 64 (2025): 202424184, https://doi.org/10.1002/anie.202424184.

39. X. Jiang, Q. Zhang, N. Zhao, Z. Li, L. Jiang, and Z. Zhang, "2D Conjugated Metal–Organic Framework-Based Composite Membranes for Nanofluidic Ionic Photoelectric Conversion," *Advanced Materials* 37 (2025): 2416093, https://doi.org/10.1002/adma.202416093.

40. W. Xian, C. Zhu, Z. Lai, et al., "Harnessing Solar-Salinity Synergy with Porphyrin-Based Ionic Covalent-Organic-Framework Membranes for Enhanced Ionic Power Generation," *Chem & Bio Engineering* 1 (2024): 461–468, https://doi.org/10.1021/cbe.3c00119.

41. W. Xian, C. Zhu, Z. Lai, et al., "Enhancing Sustainable Energy Conversion Efficiency by Incorporating Photoelectric Responsiveness into Multiporous Ionic Membrane," *Small* 20 (2024): 2310791, https://doi.org/10.1002/smll.202310791.

42. Q. Shen, J. Chen, X. Jing, and C. Duan, "Selective Aerobic Oxidation of Toluene to Benzaldehyde by Parallel Photoinduced Proton-Coupled Electron Transfer and Energy Transfer through Multiphoton Excitation," *Angewandte Chemie International Edition* 64 (2025): 202506277, https://doi.org/10.1002/anie.202506277.

43. Q. Wang, J. Chen, H. Pan, et al., "Modulating Active Center Microenvironment in Phthalocyanine-Based Covalent Organic Frameworks for Enhanced Electrocatalytic CO_2 to CH_3 OH," *Advanced Materials* 37 (2025): 2502644, https://doi.org/10.1002/adma.202502644.

44. M. Li, T. Zhang, Y. Shi, C. He, and C. Duan, "Modifying Proton Relay into Bioinspired Dye-Based Coordination Polymer for Photocatalytic Proton-Coupled Electron Transfer," *Angewandte Chemie International Edition* 63 (2024): 202406161, https://doi.org/10.1002/anie.202406161.

45. J. Yang, Y. Liu, Z. Chen, et al., "Indole-Linkages as Base-Activated Sites in a Covalent Organic Framework for Efficient Photosynthesis of Hydrogen Peroxide under Alkaline Conditions," *Angewandte Chemie International Edition* 64 (2025): 22298.

46. S. Yang, D. Si, L. Zou, M. Shi, Y. Huang, and R. Cao, "Engineering Imine Carbon Catalytic Sites in Covalent Organic Frameworks for Enhanced Overall H_2O_2 Photosynthesis," *Journal of the American Chemical Society* 147 (2025): 30287–30295, https://doi.org/10.1021/jacs.5c09327.

47. L. Li, X. Yao, W. Ou, et al., "Triazine-cored Donor–acceptor Covalent Organic Framework Promotes Highly Efficient Photocatalytic Synthesis of H_2 O_2," *Green Chemistry* 27 (2025): 9144–9152, https://doi.org/10.1039/D5GC01754H.

48. H. Yu, F. Zhang, Q. Chen, et al., "Vinyl-Group-Anchored Covalent Organic Framework for Promoting the Photocatalytic Generation of Hydrogen Peroxide," *Angewandte Chemie International Edition* 63 (2024): 202402297, https://doi.org/10.1002/anie.202402297.

15214095, 2026, 46, Downloaded from https://advanced.onlinelibrary.wiley.com/doi/10.1002/adma.73980 by Shengqian Ma - University Of North Texas Willis Library , Wiley Online Library on [21/10/2026]. See the Terms and Conditions (https://onlinelibrary.wiley.com/terms-and-conditions) on Wiley Online Library for rules of use; OA articles are governed by the applicable Creative Commons License

49. H. Li, Y. Li, X. Lv, et al., "A Covalent Organic Framework as Photocatalyst for Smart Conversion between Photooxidation and Photoreduction and H_2O_2 Production in Full pH Environment," *Advanced Materials* 37 (2025): 2415126, https://doi.org/10.1002/adma.202415126.

50. L. Guo, L. Gong, Y. Yang, Z. Huang, X. Liu, and F. Luo, "Rational Construction of Cyanide-Functionalized D-a-π-D Covalent Organic Framework for Highly Efficient Overall H_2 O_2 Photosynthesis from Air and Water," *Angewandte Chemie International Edition* 64 (2025): 202414658, https://doi.org/10.1002/anie.202414658.

51. Z. Li, Z. Dong, Z. Zhang, et al., "Covalent Organic Frameworks for Boosting H_2O_2 Photosynthesis via the Synergy of Multiple Charge Transfer Channels and Polarized Field," *Angewandte Chemie International Edition* 64 (2025): 202420218.

52. K. H. Xie, G. B. Wang, F. Huang, et al., "Multicomponent One-Pot Construction of Benzo[f]Quinoline-Linked Covalent Organic Frameworks for H_2O_2 Photosynthesis," *Nature Communications* 16 (2025): 3493, https://doi.org/10.1038/s41467-025-58839-7.

53. J. Feng, Y. Wei, X. Li, et al., "3D-Printed COF/Zeolite Composites for Augmented Photocatalytic Hydrogen Peroxide Production," *Angewandte Chemie International Edition* 64 (2025): 202508226, https://doi.org/10.1002/anie.202508226.

54. Q. Zuo, B. Chu, X. Ye, F. Li, L. Li, and Q. Xu, "Enzyme-Click Postsynthetic Modification of Covalent Organic Frameworks for Photocatalytic H_2O_2 Production," *Journal of the American Chemical Society* 147 (2025): 34681–34689, https://doi.org/10.1021/jacs.5c09922.

55. C. Sun, Y. Han, H. Guo, et al., "Proton Reservoir in Covalent Organic Framework Compensating Oxygen Reduction Reaction Enhances Hydrogen Peroxide Photosynthesis," *Advanced Materials* 37 (2025): 2502990, https://doi.org/10.1002/adma.202502990.

56. S. Fang, Y. Liao, J. Tang, et al., "Vertical Covalent Organic Framework Interlayer Channels Enable Ultraselective Molecular Separations," *Science Advances* 11 (2025): aeb0929, https://doi.org/10.1126/sciadv.aeb0929.

57. Q. Guo, H. Guo, Z. Xing, et al., "Energy-Autonomous KCl Extraction from Brine via Biomimetic Covalent-Organic-Framework Membranes and Redox-Driven Ion Transport," *Nature Communications* 16 (2025): 11483, https://doi.org/10.1038/s41467-025-66345-z.

58. J. Qu, Y. Wang, T. Sun, et al., "Engineering Covalent Organic Frameworks for Photocatalytic Overall Water Vapor Splitting," *Angewandte Chemie International Edition* 64 (2025): 202502821, https://doi.org/10.1002/anie.202502821.

59. Z. Chen, H. Weng, C. Chu, et al., "Nitrogen Heterocyclic Covalent Organic Frameworks for Efficient H_2O_2 Photosynthesis and in Situ Water Treatment," *Nature Communications* 16 (2025): 6943, https://doi.org/10.1038/s41467-025-62371-z.

60. Q. Zhang, M. Zhou, G. Ren, Y. Li, Y. Li, and X. Du, "Highly Efficient Electrosynthesis of Hydrogen Peroxide on a Superhydrophobic Three-Phase Interface by Natural Air Diffusion," *Nature Communications* 11 (2020): 1731, https://doi.org/10.1038/s41467-020-15597-y.

61. H. Zhou, X. Sheng, J. Xiao, et al., "Increasing the Efficiency of Photocatalytic Reactions via Surface Microenvironment Engineering," *Journal of the American Chemical Society* 142 (2020): 2738–2743, https://doi.org/10.1021/jacs.9b12247.

62. Y. Li, Z. Pei, D. Luan, and X. W. D. Lou, "Triple-Phase Photocatalytic H_2O_2 Production on a Janus Fiber Membrane with Asymmetric Hydrophobicity," *Journal of the American Chemical Society* 146 (2024): 3343–3351, https://doi.org/10.1021/jacs.3c12465.

63. L. Li, L. Xu, Z. Hu, and J. C. Yu, "Enhanced Mass Transfer of Oxygen through a Gas–Liquid–Solid Interface for Photocatalytic Hydrogen Peroxide Production," *Advanced Functional Materials* 31 (2021): 2106120, https://doi.org/10.1002/adfm.202106120.

64. J. Y. Yue, L. P. Song, Z. X. Pan, et al., "Regulating the H_2O_2 Photosynthetic Activity of Covalent Organic Frameworks through Linkage Orientation," *ACS Catalysis* 14 (2024): 4728–4737, https://doi.org/10.1021/acscatal.4c00278.

65. X. Li, Y. Fu, Q. An, et al., "Micro-Modulation of Linkers of Covalent Organic Frameworks as Catalysts for 2e$^-$ Oxygen Reduction Reaction," *Applied Catalysis B: Environment and Energy* 344 (2024): 123611, https://doi.org/10.1016/j.apcatb.2023.123611.

66. J. Guo, X. H. Zhong, L. Rao, et al., "Anthraquinone-Based Donor–Acceptor Covalent Organic Frameworks with Thiazole Linkages to Enhance Direct Hydrogen Atom Transfer and Charge Separation in Photocatalytic Oxidation of C(sp_3)—H Bonds," *Angewandte Chemie International Edition* 64 (2025): 202517694, https://doi.org/10.1002/anie.202517694.

67. F. Zhang, X. Lv, H. Wang, et al., "p-π Conjugated Covalent Organic Frameworks Expedite Molecular Triplet Excitons for H_2 O_2 Production Coupled with Biomass Upgrading," *Advanced Materials* 37 (2025): 2502220, https://doi.org/10.1002/adma.202502220.

68. Y. H. Kim, J. P. Jeon, Y. Kim, et al., "Cobalt-Porphyrin-Based Covalent Organic Frameworks with Donor-Acceptor Units as Photocatalysts for Carbon Dioxide Reduction," *Angewandte Chemie International Edition* 62 (2023): 202307991, https://doi.org/10.1002/anie.202307991.

69. T. X. Luan, Q. Wei, C. Xin, et al., "Remarkably Enhancing H_2O_2 Photogeneration by Modulating Pore-Microenvironment of a Photoactive Covalent Organic Framework," *Advanced Materials* 37 (2025): 15517.

70. L. Zhang, J. Du, Z. Xie, et al., "Discovery of Highly Fluorescent Covalent Organic Frameworks through AI-Assisted Iterative Experiment–learning Cycles," *Nature Chemistry* 17 (2025): 1645–1654, https://doi.org/10.1038/s41557-025-01974-x.

71. L. Zhang, C. Wang, Q. Jiang, P. Lyu, and Y. Xu, "Structurally Locked High-Crystalline Covalent Triazine Frameworks Enable Remarkable Overall Photosynthesis of Hydrogen Peroxide," *Journal of the American Chemical Society* 146 (2024): 29943–29954, https://doi.org/10.1021/jacs.4c12339.

72. J. Yang, Z. Zhao, X. Liu, et al., "Homologous Heteropolyaromatic Covalent Organic Frameworks for Enhancing Photocatalytic Hydrogen Peroxide Production and Aerobic Oxidation," *Nature Communications* 16 (2025): 7654, https://doi.org/10.1038/s41467-025-62937-x.

73. R. M. Zhu, Y. Liu, W. K. Han, et al., "Three-Dimensional Covalent Organic Frameworks Based on Linear and Trigonal Linkers for High-Performance H_2O_2 Photosynthesis," *Angewandte Chemie International Edition* 64 (2025): 202412890.

74. P. Li, F. Ge, Y. Yang, et al., "1D Covalent Organic Frameworks Triggering Highly Efficient Photosynthesis of H_2O_2 via Controllable Modular Design," *Angewandte Chemie International Edition* 63 (2024): 202319885, https://doi.org/10.1002/anie.202319885.

Supporting Information

Additional supporting information can be found online in the Supporting Information section.

Supporting File: adma73980-sup-0001-SuppMat.docx.

15214095, 2026, 46, Downloaded from https://advanced.onlinelibrary.wiley.com/doi/10.1002/adma.73980 by Shengqian Ma - University Of North Texas Willis Library , Wiley Online Library on [21/10/2026]. See the Terms and Conditions (https://onlinelibrary.wiley.com/terms-and-conditions) on Wiley Online Library for rules of use; OA articles are governed by the applicable Creative Commons License